

Strong near-infrared emission in the sub-AU disk of the Herbig Ae star HD 163296: evidence for refractory dust?[★]

M. Benisty^{1,2}, A. Natta¹, A. Isella³, J-P. Berger², F. Massi¹, J-B. Le Bouquin⁴, A. Mérand⁴, G. Duvert², S. Kraus⁵, F. Malbet^{2,3}, J. Olofsson², S. Robbe-Dubois⁶, L. Testi⁷, M. Vannier⁶, G. Weigelt⁵

¹ INAF-Osservatorio Astrofisico di Arcetri, Largo E. Fermi 5, 50125 Firenze, Italy

² Laboratoire d'Astrophysique de Grenoble, CNRS-UJF UMR 5571, 414 rue de la piscine, 38400 St Martin d'Hères, France

³ Caltech, MC 249-17, 1200 East California Blvd, Pasadena, CA 91125, USA

⁴ European Southern Observatory, Casilla 19001, Santiago 19, Chile

⁵ Max Planck Institut für Radioastronomie, Auf dem Hügel 69, 53121 Bonn, Germany

⁶ Laboratoire A. H. Fizeau, UMR 6525, Université de Nice-Sophia Antipolis, Parc Valrose, 06108 Nice Cedex 02, France

⁷ European Southern Observatory, Karl-Schwarzschild-Strasse 2, 85748 Garching, Germany

Received 2009-07-16; Accepted 2009-11-03

ABSTRACT

We present new long-baseline spectro-interferometric observations of the Herbig Ae star HD 163296 (MWC 275) obtained in the *H* and *K* bands with the AMBER instrument at VLTI. The observations cover a range of spatial resolutions between ~ 3 and ~ 12 milli-arcseconds, with a spectral resolution of ~ 30 . With a total of 1481 visibilities and 432 closure phases, they result in the best (u, v) coverage achieved on a young star so far. The circumstellar material is resolved at the sub-AU spatial scale and closure phase measurements indicate a small but significant deviation from point-symmetry. We discuss the results assuming that the near-infrared excess in HD 163296 is dominated by the emission of a circumstellar disk. A successful fit to the spectral energy distribution, near-infrared visibilities and closure phases is found with a model where a dominant contribution to the *H* and *K* band emissions arises from an optically thin, smooth and point-symmetric region extending from about 0.1 to 0.45 AU. At the latter distance from the star, silicates condense, the disk becomes optically thick and develops a puffed-up rim, whose skewed emission can account for the non-zero closure phases. We discuss the nature of the inner disk emission and tentatively rule out dense molecular gas as well as optically thin atomic or ionized gas as its possible origin. We propose instead that the smooth inner emission traces the presence of very refractory grains in a partially cleared region, extending at least to ~ 0.5 AU. If so, we may be observing the disk of HD 163296 just before it reaches the transition disk phase. However, we note that the nature of the refractory grains or, in fact, even the possibility for any grain to survive at the very high temperatures we require ($\sim 2100 - 2300$ K at 0.1 AU from the star) is unclear and should be investigated further.

Key words. Optical interferometry – VLTI – Herbig Ae star – HD 163296 (MWC275)

1. Introduction

Herbig AeBe stars (HAeBe) are intermediate-mass young stars, surrounded by large amounts of dust and gas. The distribution of this circumstellar material is still actively debated. Various types of models can reproduce the spectral energy distribution (SED), considering material in geometrically thin accretion disks (Hillenbrand et al. 1992), in a spherical envelope (Miroshnichenko et al. 1997), in a puffed-up inner disk rim (Dullemond et al. 2001; Isella & Natta 2005) or in a disk plus halo (Vinković et al. 2006). Fitting the SED alone is therefore highly ambiguous.

In the last decade, near-infrared (NIR) long baseline interferometry has allowed us to directly probe matter within the inner astronomical unit (AU), where key quantities for the star-disk-protoplanets interactions are set. The first interferometric studies of HAeBe showed that the NIR characteristic sizes were larger than expected with classical accretion disk mod-

els (Millan-Gabet et al. 2001), and were found to be correlated to the stellar luminosity (Monnier & Millan-Gabet 2002). This supports the idea that the NIR emission is dominated by thermal emission of hot dust heated by stellar radiation. Natta et al. (2001) suggested that an inner, optically thin cavity due to dust sublimation exists in the disk. At the edge of this region, where dust condensates, the disk is expected to puff up due to direct illumination from the star (Dullemond et al. 2001; Isella & Natta 2005), explaining the size-luminosity law derived for Herbig Ae (and late Be) stars by Monnier & Millan-Gabet (2002). Based on a small number of interferometric observations, simple geometrical models were proposed to explain the global morphology of these regions (Millan-Gabet et al. 2001; Eisner et al. 2004; Monnier et al. 2005, 2006). However, when larger sets of data became available, it became clear that the regions probed by NIR interferometry are much more complex and that a deeper understanding requires the combination of photometric and multi-wavelength interferometric measurements at the milli-arcsecond resolution together with more sophisticated models.

In this study, we present an analysis of the inner disk surrounding the HAe star HD 163296 (MWC275). This isolated Herbig Ae star is well described with a spectral type of A1, a ~ 30 L_\odot luminosity and a ~ 2.3 M_\odot mass (van den Ancker et al.

Send offprint requests to: benisty@arcetri.astro.it

[★] Based on AMBER observations collected at the VLTI (European Southern Observatory, Paranal, Chile) with Arcetri Guaranteed Time program 081.C-0124, LAOG Guaranteed Time program 081.C-0794 and open time programs 081.C-0851, 081.C-0098.

1998; Natta et al. 2004; Montesinos et al. 2009). It is located at 122_{-13}^{+17} pc and exhibits a NIR excess interpreted as the emission from a circumstellar disk (Hillenbrand et al. 1992). A large-scale disk was detected in scattered light (Grady et al. 2000), as well as at millimeter wavelengths (Mannings & Sargent 1997). This inclined disk, traced up to 540 AU, was found to be in Keplerian rotation, and probably evolving towards a debris disk phase (Isella et al. 2007). In addition, it also shows an asymmetric outflow on large scales ($\geq 27''$) perpendicular to the disk, with a chain of six Herbig-Haro knots (HH409) that traces the history of mass loss (Devine et al. 2000; Wassell et al. 2006). The spectro-photometric observations that probe the intermediate and small spatial scales are also compatible with the presence of a disk. In fact, Doucet et al. (2006) studied the warm dust emitting in the mid-infrared, located in the surface layers of the intermediate regions of the disk (30–100 AU) and concluded that the emission was consistent with a disk that has little flaring. This conclusion is consistent with the classification of HD 163296 by Meeus et al. (2001) in their Group II whose SED can be explained assuming that the inner part of the disk shields the outer part from stellar radiation. In the innermost regions, the far-UV emission lines have been attributed to optically thin gas accreting onto the stellar surface, to a magnetically confined wind or to shocks at the base of the jet (Deleuil et al. 2005; Swartz et al. 2005). Weak X-ray emission ($L_x/L_\star \sim 510^{-6}$) has been detected on large scale and attributed to the jet (Günther & Schmitt 2009). In the NIR, the SED time variability was interpreted to be due to changes in the inner disk structure, on timescales similar to the generation of the HH objects (Sitko et al. 2008).

With a disk, signs of accretion and a bipolar outflow, HD 163296 provides an excellent case study to understand how the circumstellar material is distributed at the sub-AU scale. As a matter of fact, its NIR disk was resolved by IOTA, PTI, and Keck-Interferometer (Millan-Gabet et al. 2001; Eisner et al. 2009; Monnier et al. 2005), and more recently, at milli-arcsecond (mas) resolution with the long CHARA baselines (Tannirkulam et al. 2008) (T08, hereafter). T08 found that their observations could not be reproduced using models where the majority of the K band emission arises in a dust rim, but that an additional NIR emission inside the dust sublimation radius could explain the visibilities and the SED. They interpreted this additional emission as being produced by gas, as suggested for other Herbig AeBe stars (Eisner et al. 2007; Isella et al. 2008; Kraus et al. 2008b). The advent of spectro-interferometry, as provided by the AMBER instrument at VLTI, allows us to simultaneously measure the emission at various NIR wavelengths and consequently, to derive temperature profiles for the emission, bringing additional constraints on its nature. In this paper, we present an observational study of the circumstellar disk around HD 163296 at the sub-AU scale, using the largest interferometric dataset obtained on a young star so far. The paper is organized as follows: in Sect. 2, we describe the spectro-interferometric observations obtained at AMBER/VLTI and the data processing; in Sect. 3, we present the obtained visibilities and closure phases. In Sect. 4, we detail a successful disk model that reproduces all observables and discuss its physical origin. We summarize our results in Sect. 5.

2. Observations and data reduction

2.1. Observations at VLTI

HD 163296 was observed in the NIR with the AMBER instrument (Petrov et al. 2007), at the Very Large Telescope

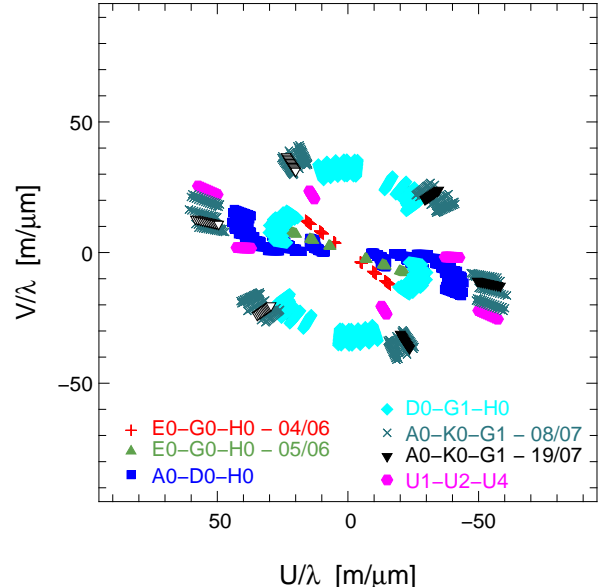


Fig. 1. (u, v) plane coverage of the observations in spatial frequencies. The observing nights are plotted with different symbols and the corresponding telescope configurations are reported in the figure.

Interferometer (VLTI; Schöller 2007), located at Cerro Paranal, Chile and operated by the European Southern Observatory (ESO). The AMBER instrument allows the simultaneous combination of three beams in the H and K bands (*i.e.* from 1.6 to $2.5 \mu\text{m}$) with spatial filtering. The instrument delivers spectrally dispersed interferometric observables (*e.g.* visibilities, closure phases, differential phases) at spectral resolutions up to 12000.

In the following, we present observations taken in the low spectral resolution mode ($R \sim 30$) with the 1.8 m Auxiliary Telescopes (AT) and the 8.2 m Unit Telescopes (UTs). The data were obtained within programs of both guaranteed time and open time observations (081.C-0794; 081.C-0098; 081.C-0124; 081.C-0851). HD 163296 was observed with 14 different baselines of 5 VLTI telescope configurations, during 8 nights from May to July 2008. The longest baseline is ~ 128 m corresponding to a maximum resolution of 3.5 mas in the K band, and of 2.7 mas in the H band. In this paper, we use the VLTI nomenclature to identify the different configurations. A summary of the observations can be found in Table 1, including the weather conditions, the average baseline position angles (B_{PA}) and projected lengths (B_L). The projected baseline is obtained when the vector between the two telescopes is projected onto the plane of the sky. Due to Earth rotation, measurements with the same physical baseline but at different hour angles correspond to different projected baselines.

All the observations were performed with three telescopes, except during the night of the 26-05-2008 when only two were available. In addition to HD 163296, three calibrator stars (HD 156897, HD 160915, HD 163955) were observed before and after each measurement on the scientific target in order to correct for instrumental effects. Their stellar parameters, including their diameters, can be found in Table 2. About 25% of the observations were performed using the VLTI fringe-tracker FINITO that uses 70% of the H band flux to measure the relative optical path difference between the light beams (Le Bouquin et al. 2008).

Table 1. Log of the interferometric observations. The seeing and τ_0 were measured at 650 nm.

Date	Spectral window [μm]	Telescope configuration	Baseline name	Projected length B_L [m]	Position angle B_{PA} [$^\circ$]	Calibrator name	Seeing [$''$]	τ_0 [ms]	FINITO
24-05-2008	[1.67-1.80]-[2.06-2.42]	AO-D0-H0	A0-D0	26.7	81.6	HD156897	1.0	3.9	Y
			D0-H0	53.5	81.6				
			A0-H0	80.2	81.6				
26-05-2008	[1.62-1.79]-[2.05-2.31]	D0-G1-H0	D0-G1	69.7	138.2	HD156897	0.8	4.4	Y
04-06-2008	[1.60-1.82]-[2.03-2.33]	E0-G0-H0	E0-G0	14.3	56.5	HD156897	0.6	3.9	N
			H0-G0	28.7	56.5				
			E0-H0	43.0	56.5				
05-06-2008	[1.61-1.82]-[2.02-2.29]	E0-G0-H0	E0-G0	15.9	71.1	HD156897	0.8	4.1	N
			H0-G0	31.7	71.1				
			E0-H0	47.7	71.1				
24-06-2008	[1.65-1.80]-[2.02-2.33]	U1-U2-U4	U1-U2	55.8	33.7	HD156897	1.1	1.4	N
			U2-U4	82.6	89.8				
			U1-U4	122.8	67.6				
06-07-2008	[1.63-1.79]-[2.01-2.45]	D0-G1-H0	D0-H0	60.2	70.4	HD160915	1.0	2.3	N
			D0-G1	69.2	137.1				
			G1-H0	71.4	7.6				
08-07-2008	[1.60-1.82]-[2.01-2.44]	A0-K0-G1	A0-G1	81.4	121.6	HD160915	0.8	2.9	N
			G1-K0	86.5	29.9				
			A0-K0	108.4	74.9				
19-07-2007	[1.61-1.80]-[2.06-2.42]	A0-K0-G1	A0-G1	82.4	124.6	HD156897	1.0	1.6	N
			G1-K0	88.6	32.7				
			A0-K0	115.2	77.6				

Table 2. Star and calibrator properties. The latter have been chosen with SearchCal (<http://www.jmmc.fr/searchcal.page.htm>) and getCal (<http://mscweb.ipac.caltech.edu/gcWeb/gcWeb.jsp>)

Star	<i>V</i>	<i>K</i>	<i>H</i>	Spectral Type	Diameter [mas]
HD 163296	6.9	4.8	5.5	A1Ve	/
HD 156897	4.4	3.1	3.1	F2	0.8 ± 0.2
HD 160915	4.9	3.8	3.9	F5V	0.7 ± 0.1
HD 163955	4.7	4.5	4.6	B9V	0.3 ± 0.2

2.2. Photometry

In addition to this interferometric dataset, we collected recent photometric data from the literature (Tannirkulam et al. 2008; Sitko et al. 2008).

2.3. Data reduction

The interferometric data reduction was performed following Tatulli et al. (2007), using the `amplib` package (release 2.1) and the `yorick` interface provided by the Jean-Marie Mariotti Center (JMMC). This led to spectrally dispersed raw visibilities and closure phases for all exposures of each observing file. Not all exposures turned out to give useful data. In several cases, instrumental jitter, insufficient fringe tracking and unsatisfactory light injection into the instrument led to low contrast interferograms of our rather faint source, and we had to select the good exposures. Various selection thresholds were examined based on the fringe signal to noise ratio (SNR) criterion and led to the same absolute values for the interferometric observables. On the other hand, their accuracy changes with varying selections, and the best case (*i.e.* with the smallest errors) was obtained with a 20% and 80% best exposures selections for the squared visibilities and the closure phases respectively. In addition, data obtained at very high airmass with unstable fringe tracking were removed. No selection based on the optical path difference (*i.e.* piston) was performed, since the numbers of useful exposures

could have been a possible source of bias.

For each night, special care was given to the calibration and stability of the AMBER+VLTI instrumental transfer function through the whole observing period. Measurements of HD 163296 were encircled with observations of targets of known diameters (see Table 2) and the transfer function was interpolated along all calibrations of the night. The errors of the calibrated spectral visibilities and closure phases include the statistical errors obtained when averaging the individual exposures as well as the errors on the calibration star diameters. In order to account for the variation of the transfer function with time, we quadratically added the dispersion over the calibrator measurements to the errors. The latter is the effect that dominates the error budget.

With 8 to 14 spectral channels in the *K* band and 5 to 8 in the *H* band, the total data set (after processing) is made of 1000 and 304 spectrally dispersed *K* band visibilities and closure phases, respectively, and 481 and 128 *H* band visibilities and closure phases, respectively. The processed data will be made available for the community in the OI-FITS format (Pauls et al. 2005) on the OL BIN website (<http://olbin.jpl.nasa.gov>) in January 2010.

3. Results

The set of interferometric data presented in this paper is by far the largest for a single pre-main sequence star. The corresponding (*u*, *v*) plane coverage is shown in Fig. 1. In this section, we present a summary of the results and describe the main characteristics of the inner region of HD 163296 as revealed by NIR interferometry. For the sake of clarity, we separate the *H* and *K* band results in most of the figures below.

3.1. Visibilities

Figure 2 presents the spectral visibilities as function of the spatial frequency (*i.e.* the ratio of the projected baseline length over the wavelength of the observation). Figure 3 similarly shows

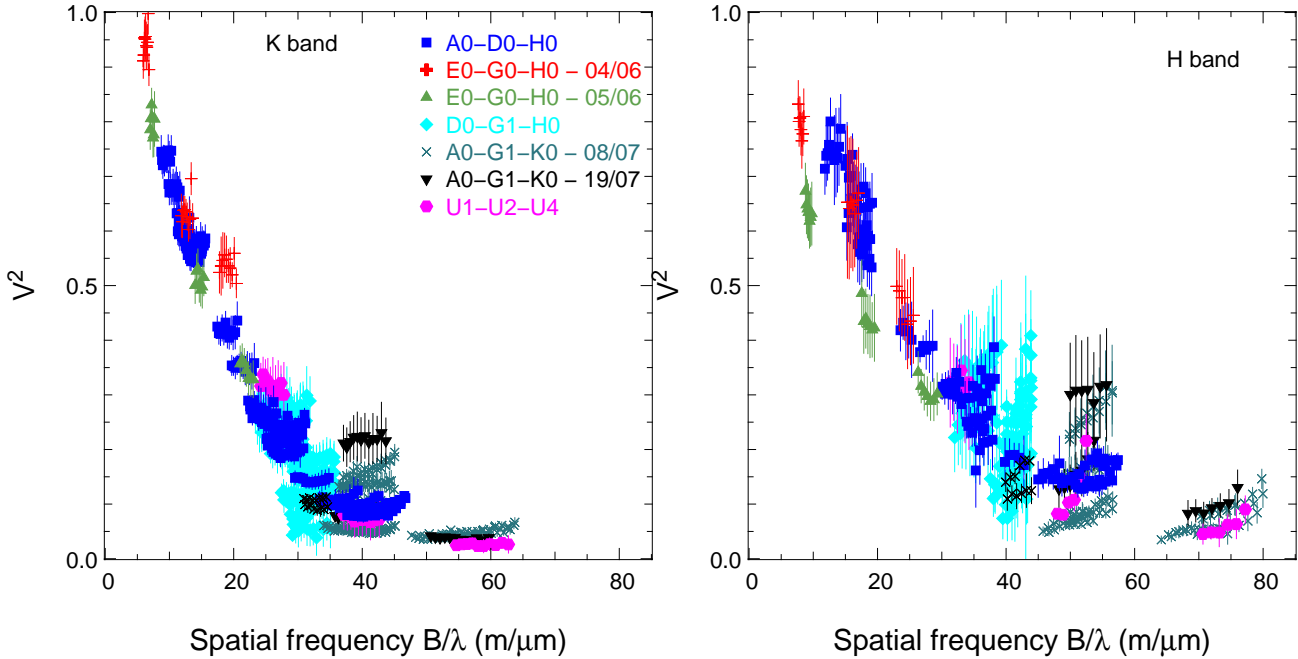


Fig. 2. Squared visibilities against spatial frequencies B/λ in the K band (left panel) and the H band (right panel). Different symbols correspond to different configurations, that are reported in the upper right corner of the left panel.

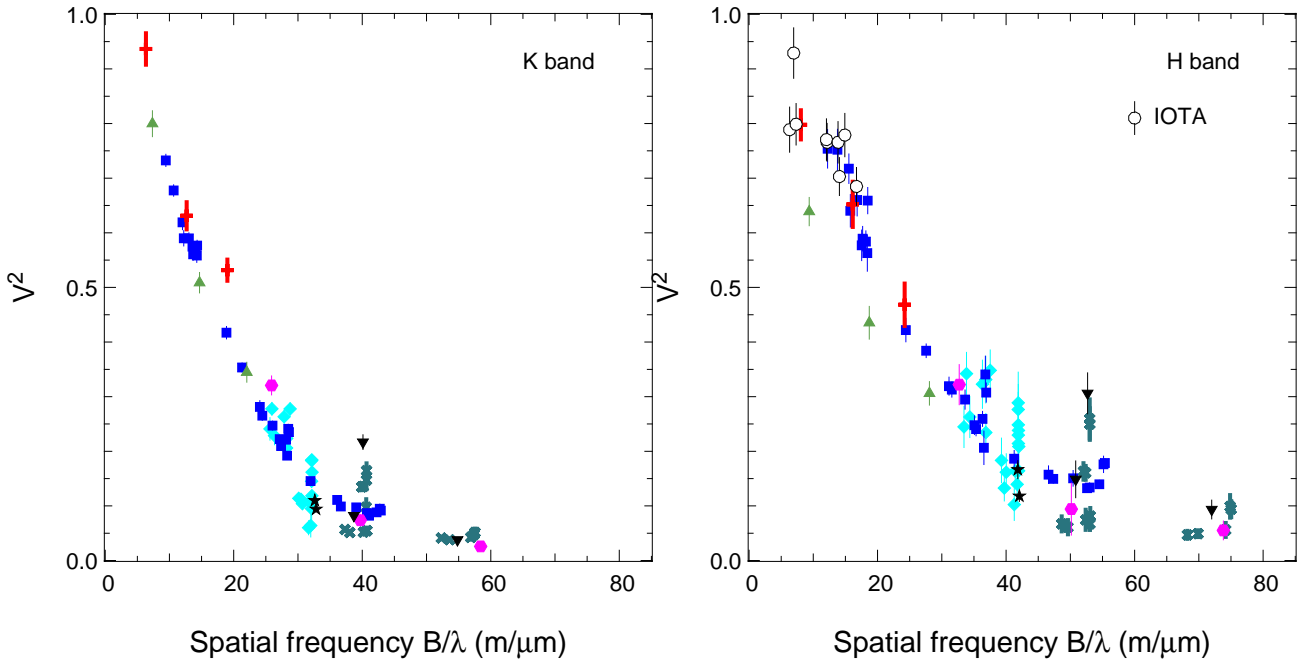


Fig. 3. Broad-band squared visibilities against spatial frequencies B/λ in the K band (left panel) and the H band (right panel). Different symbols and colors correspond to different configurations that are given in Fig. 2. The IOTA points are overplotted in the right panel (empty circles).

broad-band visibilities, obtained when averaging over all spectral channels, for the K band (left) and the H band (right). One can immediately see from the figures that at these spatial resolutions, the circumstellar matter around HD 163296 is resolved. Within the error bars, the H band visibilities vary with baseline qualitatively as the K band ones. However, at spatial frequencies larger than 20 m/μm, the H band V^2 are at least 25% higher than the ones in the K band.

The errors on individual points vary significantly from night to night. However, some of the scatter is not due to the uncer-

tainties on individual measurements, since different observations were made with baselines of similar projected baselines (equivalently, at similar spatial frequencies) but different position angle, therefore sampling distinct orientations on the sky. This effect means that the source geometry deviates from a circular one, and can instead present an elongated shape, as expected for an inclined disk.

We note that in the H band, at the shortest spatial frequencies (below 10 m/μm), the AMBER visibilities do not reach unity. This can be due to flux from an extended halo as suggested by

Monnier et al. (2006) from their IOTA H band measurements. The IOTA points, except one, are consistent with our measurements (see Fig. 3, right). On the other hand, such an effect is not clearly seen in the K band, with visibilities close to unity at short baselines (e.g. $V^2=0.94\pm0.03$ at a 13.8 m baseline).

The observations show that V^2 also depends on wavelength (Fig. 2). This can be related to the physical extension of the emitting region at various wavelengths, and to the existence of temperature gradients within it. Since the interferometer resolution also changes with wavelength, it is natural to visualize this dependence using a geometrical model to convert the measurements in angular sizes while taking into account this effect. To this goal, we fit the V^2 in each spectral channel for each measurement, using a ring of uniform brightness (with a 20% thickness). Although the circumstellar material is mainly responsible for the emission in the H and K bands, the star also contributes to the measured fluxes and visibilities. We estimate a contribution from the stellar photosphere of $\sim 33\%$ in H and $\sim 14\%$ in K (see Sect. 4.1 for details). The flux from the circumstellar matter was then computed for each AMBER channel as the difference between the observed NIR flux (T08) and the photospheric flux. Figure 4 gives an example of the wavelength dependence of the size obtained on the three baselines of the A0-D0-H0 configuration, in the two extremes cases (observed maximum and minimum variations with wavelength).

For the majority of the measurements (except the ones obtained at very small baselines with the E0-G0-H0 configuration), the size of the circumstellar matter slightly increases with wavelength. To quantify the wavelength dependence of the visibility, we studied its variation over the K band only, over the H band only, and over both bands together. Across the K and H band separately, respectively 24% and 31% of the measurements show a chromaticity above the 2σ level. Over the whole spectral range, a stronger effect is expected due to the greater wavelength interval, 62% of the data show a chromaticity larger than the 2σ level. This is consistent with the case shown in Fig. 4, where the characteristic size of the emitting region increases between the H and K bands. This trend is also observed in the spectrally dispersed measurements across the Br_γ emission line obtained with the Keck-Interferometer (Eisner et al. 2009).

3.2. Closure phases

The closure phase is a quantity that can be derived from interferometric observations with at least 3 telescopes. By summing up the phases of the fringes obtained with 3 telescopes, the atmospheric disturbances are cancelled out. Consequently, the sum of the three phases (the closure phase) is atmosphere-free, *i.e.*, independent of the phase fluctuations. It is related to the degree of asymmetry of the observed brightness distribution: a point-symmetric object will have zero closure phases while a non-zero measurement implies a deviation from point-symmetry. The sign of the CP is derived from the way it is calculated (clockwise or counterclockwise). Physically, the CP depends on the directions that are sampled by the individual baselines of the configuration since they probe different asymmetries of the brightness distribution, which in turn strongly depend on the flux ratio between the star and the circumstellar matter.

One or more closure phase (CP) measurements were obtained for each observing night, except for the night of 26-05-2008. In total, we obtained 304 CP in the K band, and 128 in the H band. This is an enormous improvement over the existing datasets for a young star. The full set of measured CP across the K and H bands is shown in Fig. 5, plotted against the maximum

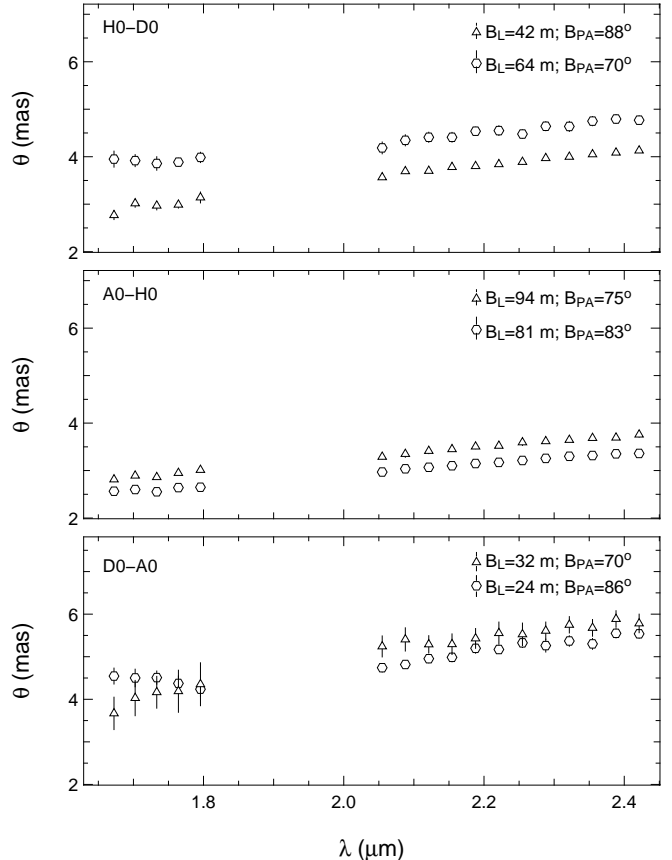


Fig. 4. Example of wavelength dependence for the squared visibilities obtained on the three baselines during observations with the A0-D0-H0 configuration. In each panel, the characteristic size of the emission is given at each wavelength across the H and K band. These sizes are derived from a ring model of uniform brightness in order to account for the change of resolution with wavelength. The triangles show the maximum chromaticity over the whole wavelength range while the circles give the minimum variation. For each measurement, the corresponding projected baseline length and position angle are indicated in the top right corner.

spatial frequency B_{\max}/λ . B_{\max} refers to the projected length of the longest baseline in the corresponding configuration.

The CP signal depends on the spatial resolution achieved by the interferometer (unresolved sources are centro-symmetric). Figure 6 gives the broad-band CP in K and H plotted against the maximum spatial resolution λ/B_{\max} , achieved with the corresponding three-telescope configuration. It can be seen that the level of the CP signal increases with the power of resolution (see, for example, the configurations of aligned telescopes along the same B_{PA} , E0-G0-H0 and A0-D0-H0). Table 3 gives the corresponding broad-band CP averaged over all the measurements as well as the achieved maximum spatial resolution for each telescope configuration. As we checked that all the CP were calculated in the same way, the relative signs between measurements obtained with various configurations are relevant and should be reproduced by model fitting.

The CP is close to zero for the short linear array (E0-G0-H0): we do not detect any meaningful deviations from zero (*i.e.* any flux asymmetries) at these low spatial resolutions (10.8 and 8.5 mas in the K and H band respectively). Monnier et al. (2006) detected CP signals below $\leq 5^\circ$ for 12 Herbig AeBe stars with the

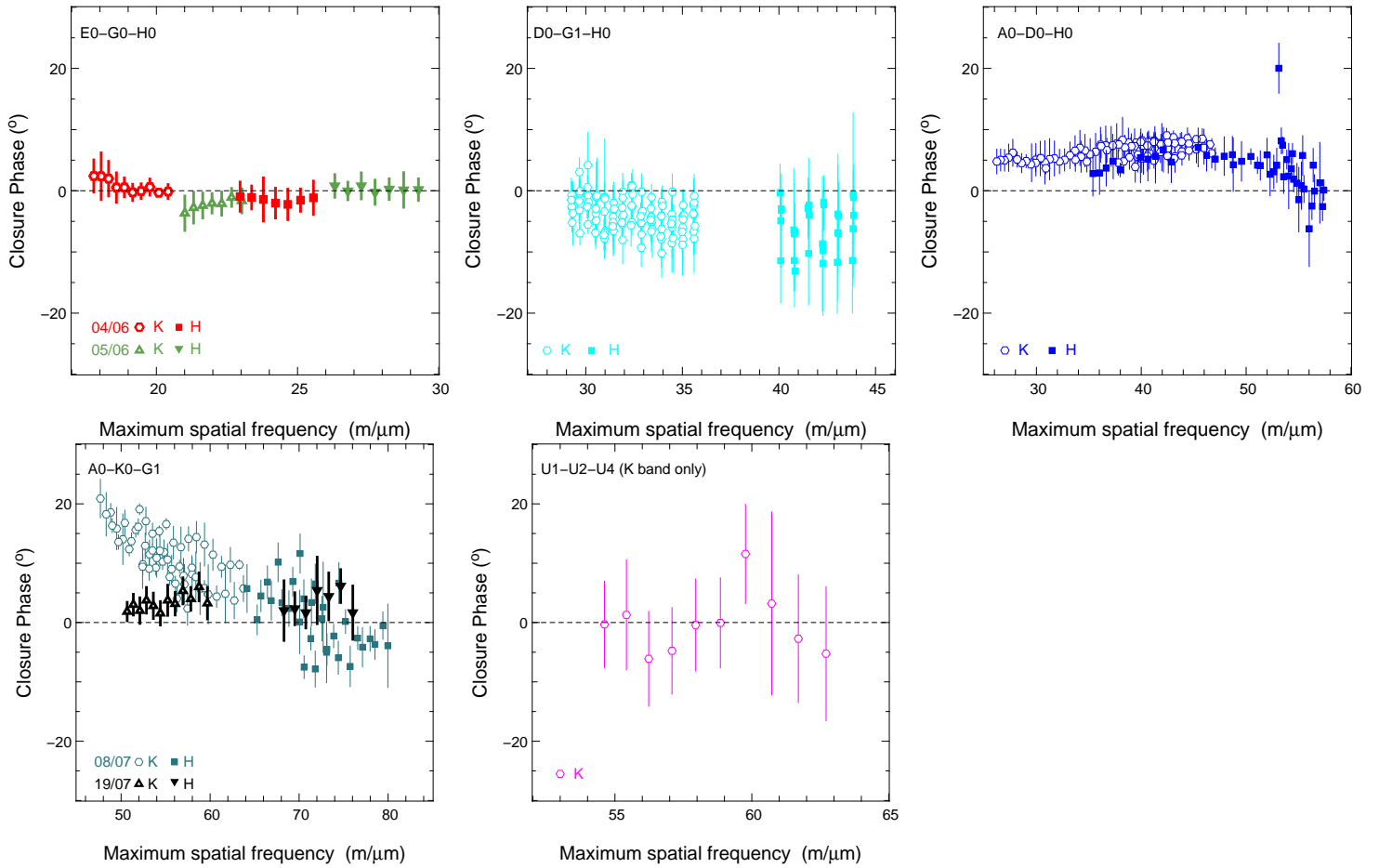


Fig. 5. Measured closure phases for each configuration (reported in the top left corners) plotted versus maximum spatial frequency. In all panels, except for U1-U2-U4 for which only *K* band data were useful, the measurements include both the *H* and *K* bands.

IOTA-3T interferometer, including HD 163296 for which they derived $0.6 \pm 0.4^\circ$ at a resolution of 11.8 mas. Our observations at similar resolution give comparable results.

At higher resolutions, we found that the CP signal is not zero, *i.e.* that the emission is no longer centro-symmetric. However, the departure of the closure phase signals from zero is small, with a maximum average CP in *K* band of $11.7 \pm 2.9^\circ$ and in *H* band of $-5.8 \pm 2.5^\circ$ (see Table 3). As we will discuss in the following section, this level of asymmetry is not compatible with strongly skewed distributions for the circumstellar material in the innermost regions surrounding the star.

Except in one case (A0-K0-G1), the CP does not vary much with varying hour angle (see Fig. 12). This means that, considering the change in maximum resolution and position angle that occurs when varying the hour angle (*i.e.* when changing the direction and the projected baseline length B_L), the level of asymmetry does not change much. Consequently, the circumstellar matter must have a rather smooth azimuthal brightness distribution.

The *H* band CP are slightly lower than the ones measured in the *K* band, as expected since the emission in *H* is likely coming from a more compact region, as most of our data suggest, than the one emitting the *K* band flux. However, considering the large error bars, this effect is hardly significant. Over the *K* band and *H* band separately, respectively 12% and 15% of the CP show a variation above the $1-\sigma$ level and all measurements are consistent with variations within the $2-\sigma$ level. Considering the whole

Table 3. Values of the closure phase as averaged over all the measurements obtained with the various configurations. The dates of the observations, the wavelength range as well as the achieved maximum spatial resolution are reported.

Configuration	Date	Band	Resolution [mas]	CP (°)
A0D0H0	24/05/08	<i>K</i>	7.9	6.5 ± 1.4
		<i>H</i>	5.8	4.3 ± 1.8
	04/06/08	<i>K</i>	11.6	0.0 ± 2.1
		<i>H</i>	9.0	-1.5 ± 1.3
E0G0H0	05/06/08	<i>K</i>	10.0	-2.0 ± 1.7
		<i>H</i>	7.9	0.2 ± 1.1
	24/06/08	<i>K</i>	3.8	-0.5 ± 10.1
		<i>H</i>	7.0	-3.3 ± 1.6
D0H0G1	06/07/08	<i>K</i>	5.1	-5.8 ± 2.5
		<i>H</i>	3.3	11.7 ± 2.9
	08/07/08	<i>K</i>	3.2	0.3 ± 4.6
		<i>H</i>	4.1	3.2 ± 2.6
A0K0G1	19/07/08	<i>K</i>	3.0	3.3 ± 3.7
		<i>H</i>		

range of wavelength (*H* and *K* together), 45% of the CP show a variation with wavelength above the $2-\sigma$ level.

4. Modelling the interferometry results

The analysis of visibilities and closure phases requires the assumption of a model for the brightness distribution on the plane

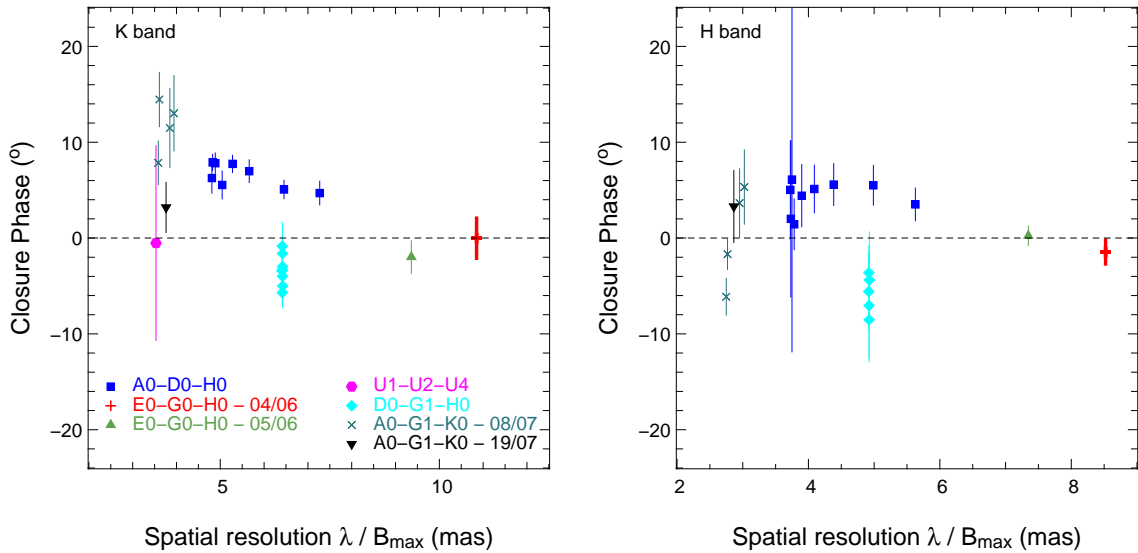


Fig. 6. Broad-band closure phases plotted against the maximum spatial resolution achieved for all telescope configurations (*K* band, left; *H* band, right). The configurations and the corresponding symbols are reported at the bottom of the left panel.

of the sky to be compared with the observations. Even when the comparison is successful, it is impossible to know if the solution is unique, and because models are heavy to compute, it is practically impossible to explore all possibilities. Here, we are guided by the current paradigm that the NIR emission in excess to the photospheric one is due to the inner parts of a circumstellar disk.

4.1. Stellar parameters

In order to model the interferometry results, one needs to know the unresolved contribution of the star to the total flux at the wavelength of interest. We compute it from the observed magnitude in the I band (*i.e.* 6.71 ± 0.026 , with very little variability over a period of about 20 years (de Winter et al. 2001; Tannirkulam et al. 2008)), assuming ZAMS colors for a A1 star and an extinction $A_V = 0.25$. The resulting stellar fluxes are about 1.4 Jy in K and 2.2 Jy in H. The observed NIR fluxes display a moderate variability (Sitko et al. 2008), so that the stellar contribution may be in the interval 14–18% in K and 33–37% in H, respectively. The effect of variability on the interferometry results and the desirability to perform simultaneous photometry have been discussed by Sitko et al. (2008). This, unfortunately, is practically impossible with AMBER/VLTI, and we do not know the values of the total flux at the time of the observations. In this paper, we adopt a stellar contribution of $\sim 14\%$ and $\sim 33\%$ to the observed *K* and *H* band fluxes, respectively, *i.e.* on the lower side of the estimates. These numbers are in agreement with the CHARA and AMBER measurements at long baselines, where all the circumstellar matter is supposedly resolved, and are similar to the values adopted by Tannirkulam et al. (2008). The HD 163296 SED is shown in Fig. 8 and 9.

4.2. Incoherent flux

In our models, we consider incoherent flux possibly emitted by an extended halo, as first suggested by Monnier et al. (2006). They estimate its contribution to be 5% of the total *H* band fluxes (*i.e.* 10% in V^2), a value that T08 also used when modelling their *K* band data. Our *H* band data suggest a slightly larger value of $\sim 8\%$ (*i.e.* $\sim 15\%$ in V^2). We adopt this value when fitting both the

H and *K* band interferometric observations. The exact origin of this emission is unknown and discussing it is beyond the scope of this paper.

4.3. Disk position angle and inclination

Values of inclination (i) and position angle (PA) of the HD 163296 disk (*i.e.*, its major axis) have been derived at different wavelengths with a variety of techniques and tend to agree: Wassell et al. (2006) ($i=51^{\circ+11}_{-9^{\circ}}$; PA= $139^{\circ}\pm15^{\circ}$), Isella et al. (2007) ($i=46^{\circ}\pm4^{\circ}$; PA= $128^{\circ}\pm4^{\circ}$) and T08 ($i=48^{\circ}\pm2^{\circ}$; PA= $136^{\circ}\pm2^{\circ}$). They are also consistent with our visibility data, which give an inclination of $40^{\circ}\pm10^{\circ}$ and a position angle of $140^{\circ}\pm15^{\circ}$, when fitted with geometrical models of an uniform brightness ring. Since we do not constrain these parameters better, we adopt in the following the values derived by T08, *i.e.* $i=48^{\circ}$ and PA= 136° . Moreover, in the next sections, we use the effective baseline, that is defined as :

$$B_{\text{eff}} = B \sqrt{\cos^2(\theta) + \cos^2(\Phi) \sin^2(\theta)}$$

where θ is the angle between the baseline direction and the major axis of the disk, and Φ is the disk inclination (T08). This representation allows us to show the data in a concise way once the inclination and position angle of the disk are known.

4.4. A disk rim

Early NIR interferometric studies of Herbig Ae stars have shown that standard accretion disks, extending up to the dust sublimation radius do not fit the observations (Millan-Gabet et al. 2007) and that better fits are obtained assuming that the disk develops a curved rim, probably (but not necessarily) controlled by dust sublimation and its dependence on gas density (Isella & Natta 2005; Tannirkulam et al. 2007). Not only the disk rim hypothesis is supported by physical calculations (Dullemond et al. 2001; Isella & Natta 2005) but the overall properties of HD 163296 are consistent with this model. In fact, the SED looks consistent as resulting from a rim emission up to $7\text{--}8\ \mu\text{m}$ and from a disk in the shade at longer wavelengths (Dullemond et al. 2001; Isella et al. 2007). In addition, our measured visibilities show a dependence

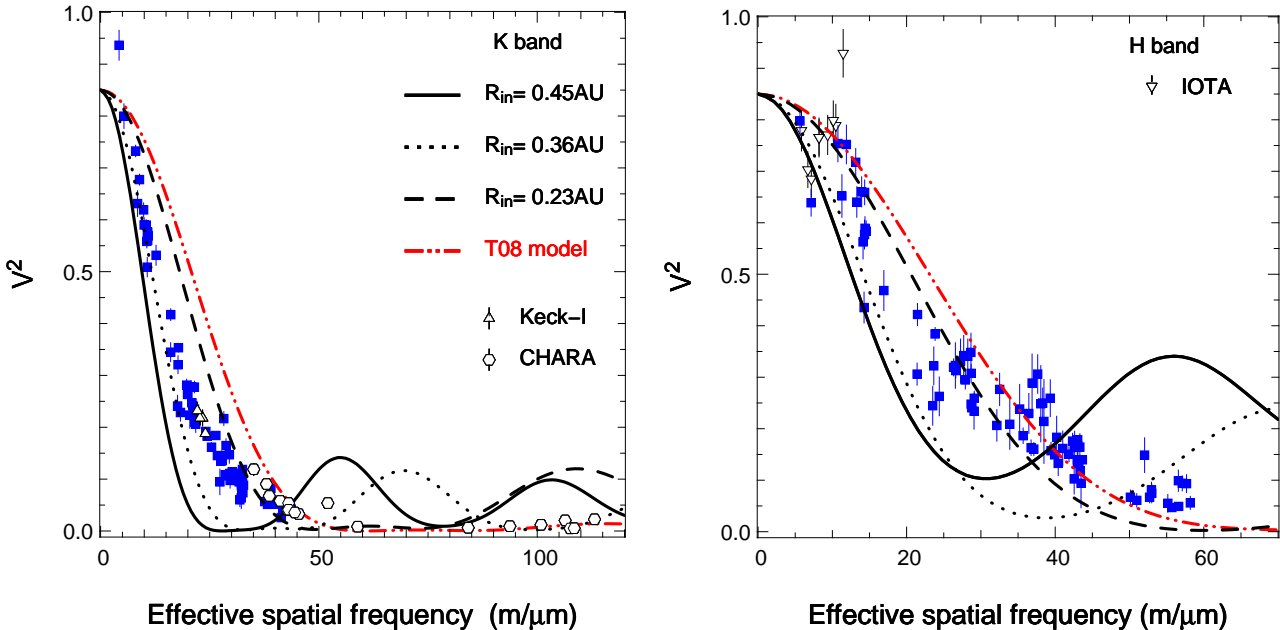


Fig. 7. Model visibilities when considering a rim alone, located at 0.23, 0.36 and 0.45 AU (dashed red, dotted blue and full black lines respectively), against effective spatial frequency B_{eff}/λ , compared to the measured broad-band visibilities (blue full squares) in the K band (left) and the H band (right). The predictions of the model described in T08, that includes an additional inner component interpreted as gas, is given in red (T08; dash-dot-dot). The K band measurements obtained at CHARA and Keck-I are overplotted (circles and triangles respectively) in the left panel, as well as the IOTA H band data (triangles) in the right panel. An incoherent flux contributing to $\sim 8\%$ of the total H and K band fluxes is considered.

on hour angle (or similarly on baseline position angle B_{PA}) consistent with an elliptical shape, as expected in a rim or in any axisymmetrical distribution seen at high inclination. Finally, the detection of non-zero closure phases supports the idea that an asymmetric brightness distribution - such as the disk inner rim - contributes to the NIR emission.

As in the NIR, the contribution of the disk outside the rim can be neglected (Isella et al. 2007), we start examining a star + rim system to model the NIR emission following Isella & Natta (2005). We adopt a stellar luminosity and mass of $30 L_{\odot}$ and $2.3 M_{\odot}$, respectively, and an effective temperature of 9250 K. The disk is assumed to be in hydrostatic equilibrium. The dust is made of silicates, with optical properties given by Weingartner & Draine (2001). The evaporation temperature, around 1500 K, depends on the local gas density as in Pollack et al. (1994). Since the shape of the rim is controlled by the largest grains, we consider a single size for the silicate dust, which therefore is the only free parameter in the model. The dependence of the evaporation temperature on z implies that the distance from the star at which dust evaporates increases with z i.e. that the rim is curved.

As it can clearly be seen in Fig. 7, our interferometric measurements are not consistent with a circumstellar emission produced by a rim only, no matter its location. This figure shows the AMBER broad-band visibilities as a function of the effective spatial frequency B_{eff}/λ . In addition to the AMBER data, we include the K band visibilities obtained at CHARA (circles; Tannirkulam et al. 2008) and at Keck-I (triangles; Monnier et al. 2005) as well as the H band IOTA data (upside down triangles; Monnier et al. 2006). We stress that all measurements from these four interferometers are compatible with each other within their error bars. The results for three rim models computed with $30 L_{\odot}$ as stellar luminosity and silicate grain sizes of 3, 0.6 or 0.3 μm , corresponding to inner rim radii at 0.23, 0.36 and 0.45 AU, re-

spectively, are overplotted. These models produce an emission that does not exceed the observed flux at any wavelength, and respectively contributes to about 80, 50 and 28% of the observed emission in H , and 91, 86, 66% in K . All models show large departures from the observations. In addition, all these models have a very asymmetric emission, and produce a closure phase signal larger than observed (see Fig. 12, red dashed lines). Our large sets of data, including H and K visibilities and closure phases, reinforce the conclusions of other authors, namely that an additional, symmetric emission closer to the star is required (T08).

4.5. A bright inner disk

A rim alone can not reproduce our observations. As a matter of fact, the lack of bounces in the visibilities suggests a continuous and smooth distribution of matter in the inner regions of HD 163296, and a low contribution of the rim to the NIR emission. In the following, we will explore the effect of adding the emission from an inner disk (inside the rim) to the star and rim contributions. We fix the rim location at $R_{\text{rim}}=0.45$ AU. Such a large radius is suggested by the results of our three-component models, as we will show in the following. It can, for example, be obtained using small silicate grains (from 0.05 to 0.5 μm) in a high-density dusty disk, or micron-sized grains in a low-density region, where the evaporation temperature will be lower. In both cases, the rim effective temperature is quite low ($T_{\text{eff}} \sim 1000$ K) and accounts for the total observed flux in the wavelength range 4-8 μm , but not at shorter wavelengths (see Fig. 8, cyan dashed line). The SED of the proposed additional inner disk can be computed subtracting the stellar and the disk rim fluxes from the observed ones. As shown in Fig. 8 (dotted line), it peaks in the H band and is higher than the rim emission at all wavelengths shorter than about 2.5 μm . Therefore, the NIR emission is dominated by the inner disk component rather than by the rim.

We obtain a first estimate of the properties of the inner disk emission modeling it as a region of constant surface brightness between an inner and an outer radius. The surface brightness is constrained by the condition that the integrated flux must be equal to the flux derived from the SED for the additional component. We compute visibilities and find that these three-component models reproduce the H and K band observations quite well over the whole range of baselines if the smooth, inner emission extends between ~ 0.10 and ~ 0.45 AU. The emission can be roughly described as that of a diluted black-body with temperature ~ 1600 K and optical depth ~ 0.2 , decreasing as $\lambda^{-1.6}$ for increasing wavelength. A natural interpretation is that the emission originates in an optically thin region inside the rim. In the following sections, we will discuss the physical nature of this component.

4.5.1. An inner gaseous disk ?

Several authors have suggested that the NIR interferometers detect the emission of gas within the dust evaporation radius (Eisner et al. 2007; Isella et al. 2008; Tannirkulam et al. 2008; Kraus et al. 2008b). This interpretation presents several difficulties in the case of HD 163296, where the additional component dominates the emission in H and K , and where good observations of high spectral resolution exist over a large range of wavelengths.

Models of the emission of purely gaseous disks inside the dust sublimation radius have been computed by Muzerolle et al. (2004) for HAe stars assuming LTE opacities. For typical HAe accretion rate ($\sim 10^{-7} M_{\odot} \text{yr}^{-1}$), the inner, dust-free disk gas surface density is larger than 10^3 g/cm^2 , the gas temperature ranges from few thousand to few hundred K and the gas is fully molecular. The NIR emission is sufficiently strong that it could, in principle, account for the observations. However, as pointed out by several authors before, the models also predict many strong molecular bands (mostly water and CO overtone transitions) which are absent in the HD 163296 spectrum (see Fig. 8, left) (Najita et al. 2000, 2007). This problem is also discussed in Najita et al. (2009), in connection with the non-detection of CO overtone and water emission in the Herbig Ae, MWC480, that also presents a hot compact NIR excess previously detected with interferometry and interpreted as resulting from water (Eisner 2007).

The assumption that the gas is in LTE, however, is certainly not appropriate at least in the upper disk layers, where the stellar radiation can penetrate, ionize and dissociate matter well above the LTE predictions. However, these thin gas layers are unlikely to contribute significantly to the broad-band observed fluxes. We have computed the emission from thin layers of gas, using the code Cloudy (Ferland et al. 1998). We assumed that the region inside the rim can be described as a geometrically thin disk, heated from the outside by the star. The disk extends from 0.1 to 0.45 AU and has constant surface density. In these conditions, as long as the disk is optically thin to the stellar radiation, the gas is mostly atomic and the ionization fraction is low (e.g. < 0.01). H^- dominates the emission in the near IR. We show in Fig. 8, right, that for surface density values of 0.1, 1 and 6 g/cm^2 (all much lower than predicted by the viscous accreting disks modelled by Muzerolle et al. 2004), the continuum emission is always too weak to be significant. Increasing it further requires higher surface densities, in which cases LTE conditions are very likely reached. In fact, for $\Sigma = 6 \text{ g/cm}^2$, the mean optical depth to the stellar radiation is already of order unity. Moreover, we note that the wavelength dependence of the non-LTE continuum is

not consistent with the observations. In particular, the H- bound-free emission produces a sharp drop at $1.6 \mu\text{m}$ corresponding to its activation energy which should be seen in the HD 163296 high resolution spectra (Sitko et al. 2008), if the gas emission was higher.

T08 suggested hot gas as the physical origin of the additional inner component. We note that their models cannot reproduce our AMBER/VLTI data, mostly because of their small inner rim radius. However, we examined the possibility that the gas is heated to higher temperatures by additional energy sources. We computed the properties of the same disk model but fixing the temperature at 8000 K. In this case, the ionization fraction is high (> 0.5) and the emission is dominated by bound-free processes. The emission can be very high, but its wavelength dependence is not consistent with the observations (see Fig. 8, right).

Based on these crude considerations, we tend to exclude that the NIR flux detected by the interferometers is dominated by the emission of hot gas inside the dust sublimation radius. However, it is clear that, before this could be definitely ruled out, one needs more realistic, non-LTE models which can treat the transition from optically thin to optically thick layers, *i.e.*, from atomic to molecular gas in a dust-free environment. Such models can also be important for the interpretation of the hydrogen and helium recombination lines, which appear very strong in the models. Atomic lines - mostly hydrogen and helium ones - are often interpreted as being emitted in magnetospheric accretion columns of gas. This, however, is unlikely to be true for most Herbig Ae stars, based on the results obtained with spectro-interferometry around the Br_{γ} emission line (Kraus et al. 2008a; Eisner et al. 2009), as this line seems to be formed in most cases, in disk material closer to the star than the silicate dust sublimation radius but outside the corotation radius.

4.5.2. An inner dusty disk ?

Inside the silicate sublimation radius, not only gas but also more refractory grains can exist and contribute to the observed NIR emission. In this section, we explore the possibility that a layer of refractory grains, extending between an inner and an outer radius (inside the rim), accounts for the interferometric and photometric observations of HD 163296. We assume that the layer is optically thin in the vertical direction with surface density profile Σ_{dust} and vertical optical depth proportional to $1/r$, where r is the distance from the star (D'Alessio et al. 1999). We compute grain temperatures and emissivity in the H and K bands, and vary the inner and outer radii (R_{in} and R_{out} , respectively) as well as the optical depth of the layer. We then computed the emission, visibilities and closure phases for models that include this inner layer, the star and the rim. We consider separately three grain species known to be refractory: iron, graphite and corundum (aluminium oxides). The iron and corundum grain cross sections are computed for spherical grains from the optical constants tabulated in Pollack et al. (1994); Koike et al. (1995); Begemann et al. (1997). We use the graphite cross sections tabulated by B. Draine¹, based on the optical constants of Laor & Draine (1993). For relatively small grains, the radial temperature profile follows $\propto r^{-0.4}$ (Fig. 9, left). For comparison, we also show the temperature profile of very large grains (black-bodies), with flat opacity from the UV to the IR ($T \propto r^{-0.5}$). These models are very simple, but probably not too unrealistic. The strongest approximation concerns the dust temperature, which we compute assuming that each grain is heated by the stel-

¹ <http://www.astro.princeton.edu/draine/dust/dust.diel.html>

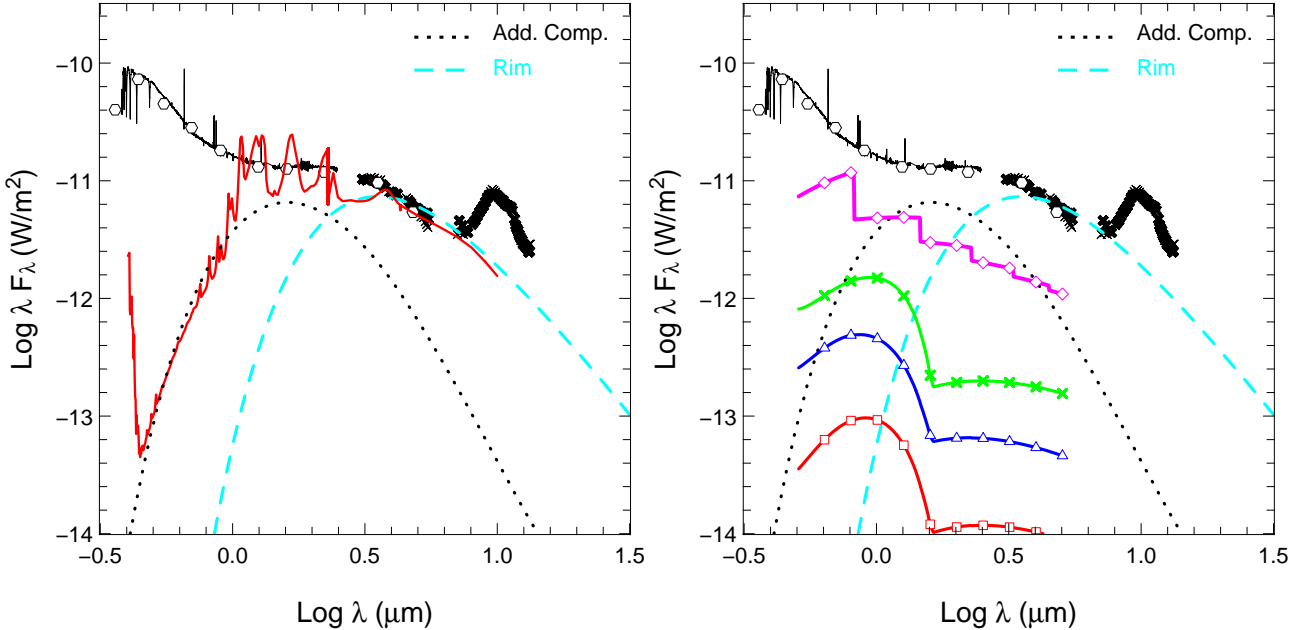


Fig. 8. SED of HD 163296 (Sitko et al. 2008; Tannirkulam et al. 2008) with the predictions of gaseous disk models. The flux emitted by the rim located at 0.45 AU (cyan dashed line) as well as the additional inner disk emission (black dotted line) are added in both panels to allow direct comparisons. Left: the predictions for optically thick and dense layers of gas in LTE (Muzerolle et al. 2004) are overplotted (red full line). In this case, the gas is mostly in molecular state. Right: the continuum emissions as predicted by thin disks of gas in non-LTE, heated from the top by the stellar radiation, are shown. The gas extends from 0.1 to 0.45 AU and has constant surface densities of 0.1, 1 and 6 g/cm² (red line with squares, blue line with triangles and green line with diamonds, respectively). In these conditions, the gas is mostly atomic. The predictions of a fully ionized layer of gas at 8000 K with a constant surface density of 0.06 g/cm² are also reported (magenta curve with diamonds). As long as the disk remains optically thin, the emission is proportional to the surface density, and this value was chosen only to display its wavelength dependence.

lar radiation, attenuated by an average optical depth $\tau_{star} \propto 0.25$, consistent with the results. In fact, the attenuation is not constant, as the optical path toward any individual grain varies not only with r but also with the incident angle of the stellar radiation. Once the temperature of the grains is known, then the emission is computed at all NIR wavelengths using a ray-tracing algorithm. As discussed in the following, a rim due to silicate condensation can form in the low density region we propose and its properties are also affected by the presence of the refractory grains in the inner disk, which absorb a small fraction of the stellar radiation. However, a self-consistent calculations of its properties is beyond the purpose of this paper. In this section, we model the rim following Isella & Natta (2005); Isella et al. (2006), assuming micron-size silicates, an evaporation temperature of ~ 1250 K and an effective stellar luminosity of 75% L_\star to account for the shielding by the inner disk. The rim radius is about 0.45 AU, and its effective temperature is about 1000 K.

We obtain a good fit to the SED as shown in Fig. 9, right, for $R_{in} = 0.10$ AU and $R_{out} = 0.45$ AU, and optical depth in the H band at R_{in} of 0.31, 0.2 and 0.25 for iron, graphite and corundum, respectively. Table 4 provides the grains properties used in these models. The total mass within 0.45 AU, which is always very low ($\leq 10^{-6} M_\oplus$), is also reported. Although we have not tried to constrain the grain parameters in any detail, we note that very large refractory grains do not give an equally good fit to the SED, as the ratio of the H over the K emission is always too large.

These models reproduce well the interferometric data, both visibilities and CP. As all three models produce similar results, we present the case for iron grains. Figure 10 shows the broad-band visibilities compared to the predictions of such a model.

Table 4. Refractory dust model parameters. For each species, the optical depths in H and K bands at 0.10 AU (R_{in}) are reported as well as the minimum and maximum grain sizes considered in the calculations. The resulting surface density Σ_{dust} and the total mass of dust grains are also given.

Species	$\tau_{K,R_{in}}$	$\tau_{H,R_{in}}$	a_{min} [μm]	a_{max} [μm]	Σ_{dust} [g cm ⁻²]	M_{dust} [M_\oplus]
Iron	0.25	0.31	0.2	2	$2.3 \cdot 10^{-4}$	$9.5 \cdot 10^{-7}$
Graphite	0.14	0.20	0.05	0.5	$2.1 \cdot 10^{-5}$	$8.7 \cdot 10^{-8}$
Corundum	0.16	0.25	0.7	5	$3.2 \cdot 10^{-4}$	$1.3 \cdot 10^{-6}$

Figure 12 presents the broad-band closure phases plotted versus hour angle together with the model predictions calculated for each telescope configuration. We overplot the predictions of the rim-alone models (red dashed line) to show how adding the optically thin dusty inner disk emission smoothes out the asymmetry induced by the rim by the right amount. Table 5 summarizes the structural parameters of this model, as derived from SED and interferometric data fitting and Fig. 11 shows the corresponding H and K band images.

The gas density of the inner disk can be derived from the values of Σ_{dust} , once the abundances of iron, carbon and aluminium in the solid species are known. Assuming, for example, that 50% of Fe is in grains, the gas surface density at 0.10 AU will be 0.2 g/cm² (0.02 g/cm² if 30% of Carbon is in graphite, or 1.3 g/cm² if all Aluminium is in corundum). The gas density can be higher if a lower fraction of the metals is condensed. However, it seems likely, from the considerations of Sect. 4.5.1, that the gas density cannot be too high. A density

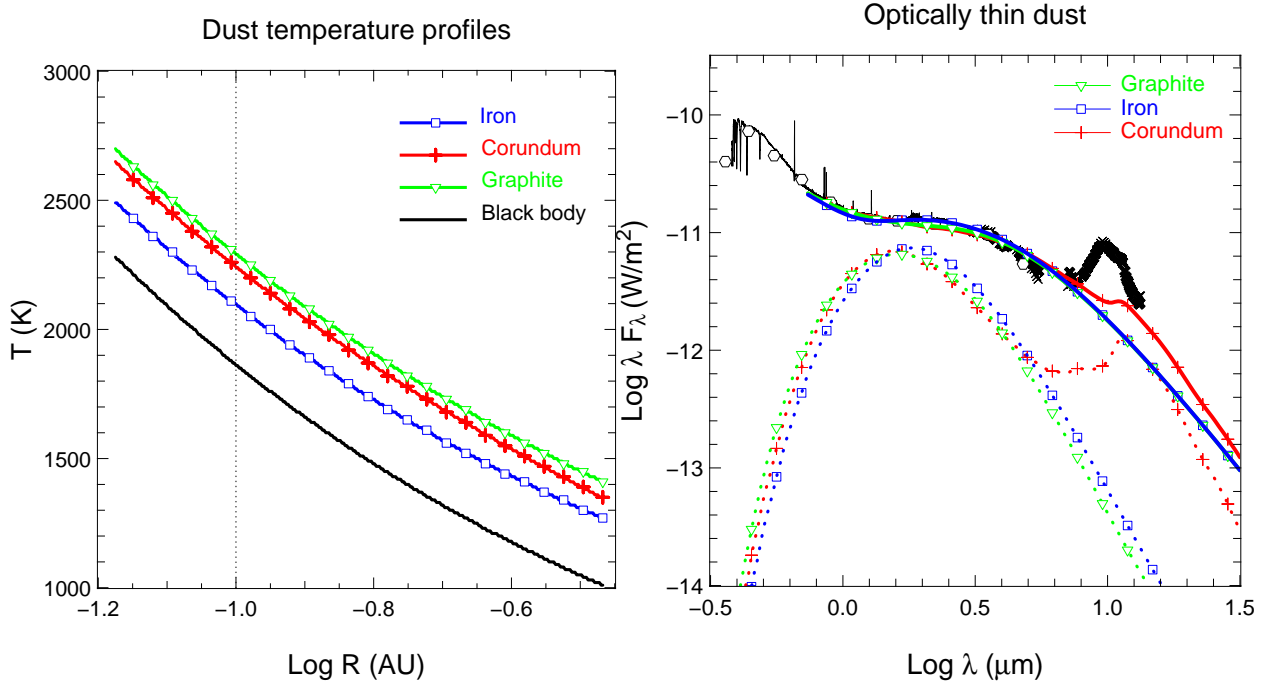


Fig. 9. Left: radial temperature profiles for graphite (green line with triangles), corundum (red line with crosses) or iron (blue line with squares). The prediction from a black body (*i.e.* large grains) is overplotted to allow comparisons. The vertical dotted line indicates 0.10 AU. Right: SED of HD 163296 together with the predictions of three models that include an inner disk made of dust to the star and the rim. The additional disk component has structural characteristics as reported in Table 5 and is made of a single refractory specie - either graphite, corundum or iron. The dotted lines give the corresponding emission while the full lines show the total flux.

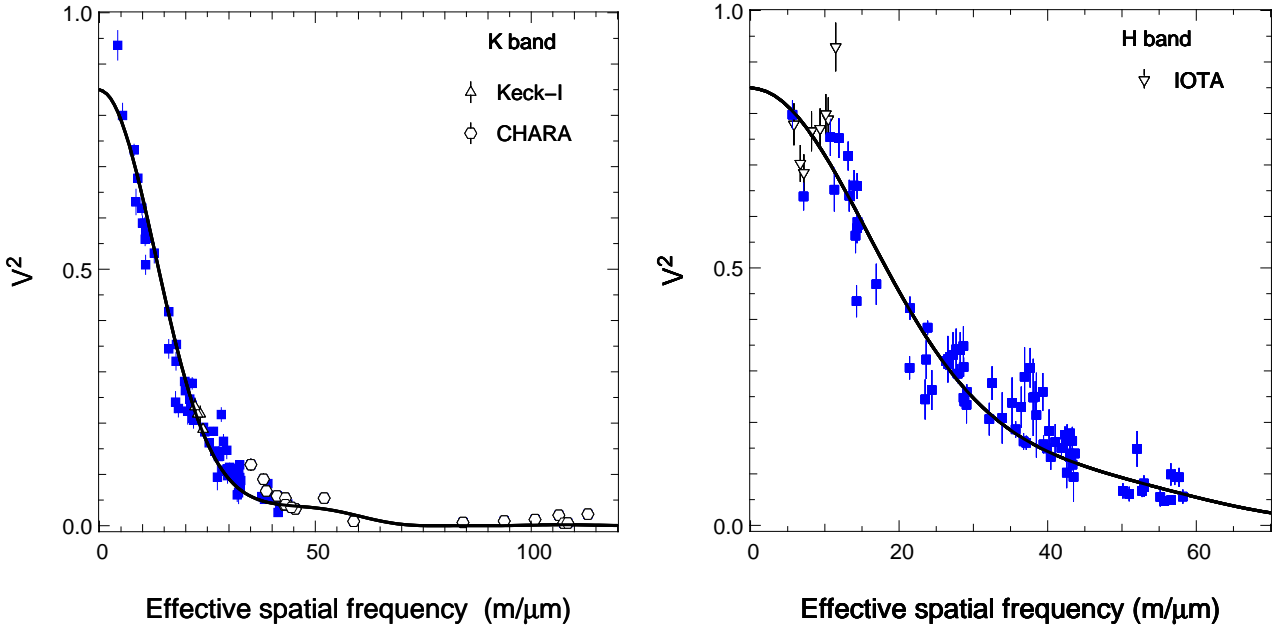


Fig. 10. Left: Visibilities as produced by our model including iron grains as responsible for the additional dusty inner disk emission, in K band (left) and H band (right) compared to the observations. The AMBER/VLTI observations (blue full squares) as well as the Keck-I (triangles) and the CHARA (circles) are added. The IOTA H band data (upside down triangles) are plotted together with the AMBER visibilities.

only a few times larger than the above lower limits is suggested by the properties of the rim in HD 163296. In particular, both the large rim radius and its low effective temperature can be reproduced in a low density disk by silicates of micron size, as inferred in several HAe stars (Isella et al. 2006), and do not

require very small grains. Assuming that the rim is due to the evaporation of silicates and that all the silicon is in olivine of $\sim 1\mu\text{m}$ size, we analyzed the rim properties in disks of increasing (but still low) surface density. For $\Sigma = 5(r/0.1\text{AU})^{-1}\text{g/cm}^2$, the *vertical* optical depth to the stellar radiation is ~ 10

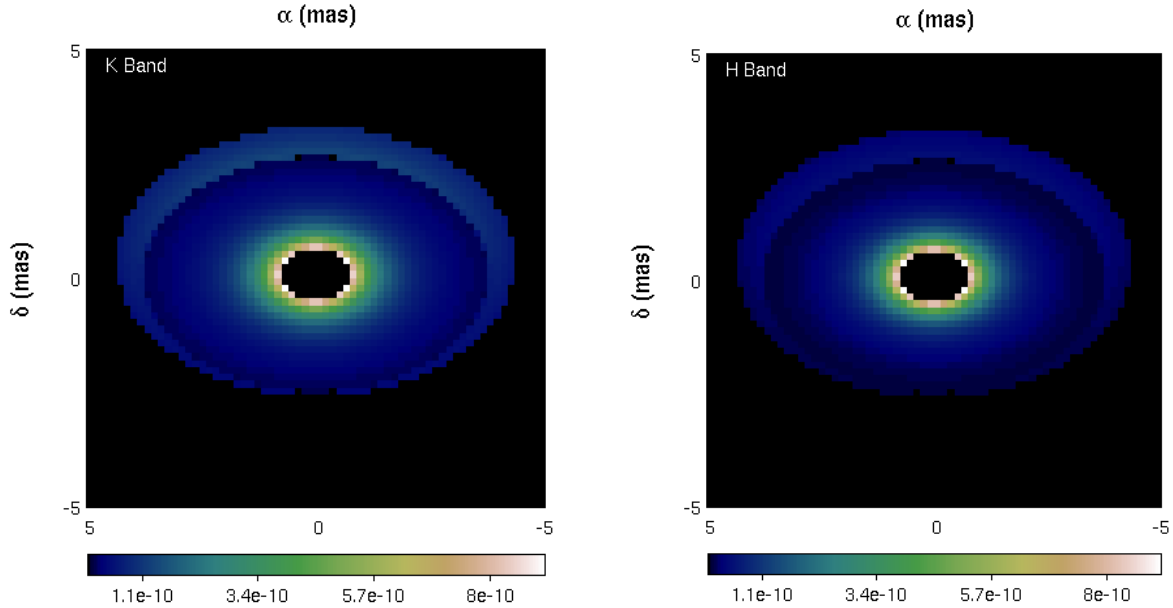


Fig. 11. Model images of the circumstellar matter surrounding HD 163296, in the case where the inner disk is constituted of refractory iron grains and a rim (outer ring). The colors are coding the flux in $\text{W} \cdot \text{s} / \text{m}^2$.

Table 5. Parameters of our model with iron grains distributed between R_{in} and R_{rim} , the location of the disk rim. For both bands, the ratio of the stellar, rim and inner disk contributions (F_* , F_{rim} and F respectively) to the total flux in the *model* (F_{tot}) are reported.

Wavelength	R_{rim} [AU]	R_{in} [AU]	T_{in} [K]	F_*/F_{tot} [%]	$F_{\text{rim}}/F_{\text{tot}}$ [%]	F/F_{tot} [%]
<i>K</i> band	0.45	0.10	2100	14	36	50
<i>H</i> band	”	”	”	30	16	54

for a gas surface density of 1 g/cm^2 at R_{rim} , large enough to allow the formation of an optically thick rim that can be modelled following Isella & Natta (2005). The low gas density, and the correspondingly low evaporation temperature, moves the rim radius further from the star. Assuming a reasonable scale height of $10^{-3} - 10^{-2} \text{ AU}$, the gas density is $\sim 10^{-11} \text{ g/cm}^3$, and the silicate evaporation temperature of the order of 1150 K. The corresponding rim radius is $\sim 0.4\text{--}0.5 \text{ AU}$, and its effective temperature is about 1000–1100 K, as required to fit the HD 163296 SED and interferometric data.

The only serious problem with the identification of the inner disk emission as coming from grains within the silicate sublimation radius, is the need for them to survive at temperatures much higher than what is generally assumed. The three types of grains we examined reach temperatures of 2100–2300 K at $\sim 0.10 \text{ AU}$ (Fig. 9, left). While similar values are possible for graphite (Krugel 2003), they are too high for iron and corundum at the pressure of our inner disk (Pollack et al. 1994; Posch et al. 2003; Kama et al. 2009). However, there is room for discussion (Najita et al. 2009), as the balance between gas and dust in the conditions of the inner disk should be re-considered in detail (Duschnl et al. 1999). We just point out that only a small amount of refractory grains has to survive these high temperatures, probably a minor fraction of the original population. The grains we

have considered are likely candidates but if other, more refractory species can form, they will certainly fit the observations equally well.

5. Summary and conclusions

This paper discusses the largest set of NIR interferometric data collected so far on a young star. HD 163296 has a well studied disk at large spatial scale, which motivated our interpretation of the NIR interferometry using a star + inner disk model. Both interferometric and photometric data can be accounted for by an inclined disk with a low density inner region. The NIR continuum emission is then not dominated by the thermal emission from the dusty disk rim located at the sublimation radius of astronomical silicates, but by the additional optically thin component located inside. This component emits about 32% of the stellar luminosity, but 54% (50%) of the observed radiation in *H* (*K*) band. Due to the silicate condensation and the strong increase of opacity, the disk rim forms in this low-density region at $\sim 0.45 \text{ AU}$ from the star and emits about 16% (36%) of the *H* (*K*) band flux. The combination of the unresolved stellar radiation, the smooth and point-symmetric emission of the inner disk region and the skewed disk rim emission can successfully explain the visibilities and non-zero closure phases measured in both bands.

The nature of the emission in the inner disk is matter of discussion. We argue against gas as being the main responsible for this continuum emission. In fact, a dense and cold disk, as expected for viscous accretion models (Muzerolle et al. 2004), would produce strong molecular lines that are not seen in high-resolution spectra. Non-LTE tenuous gas layers, in atomic state if only heating by the star is assumed, or fully ionized by additional sources of energy, can not account for the observed properties of the NIR continuum. However, we stress that self-consistent models of dust-free gaseous disks are not currently available, and that they are needed to exploit the full potential of the interferometric observations.

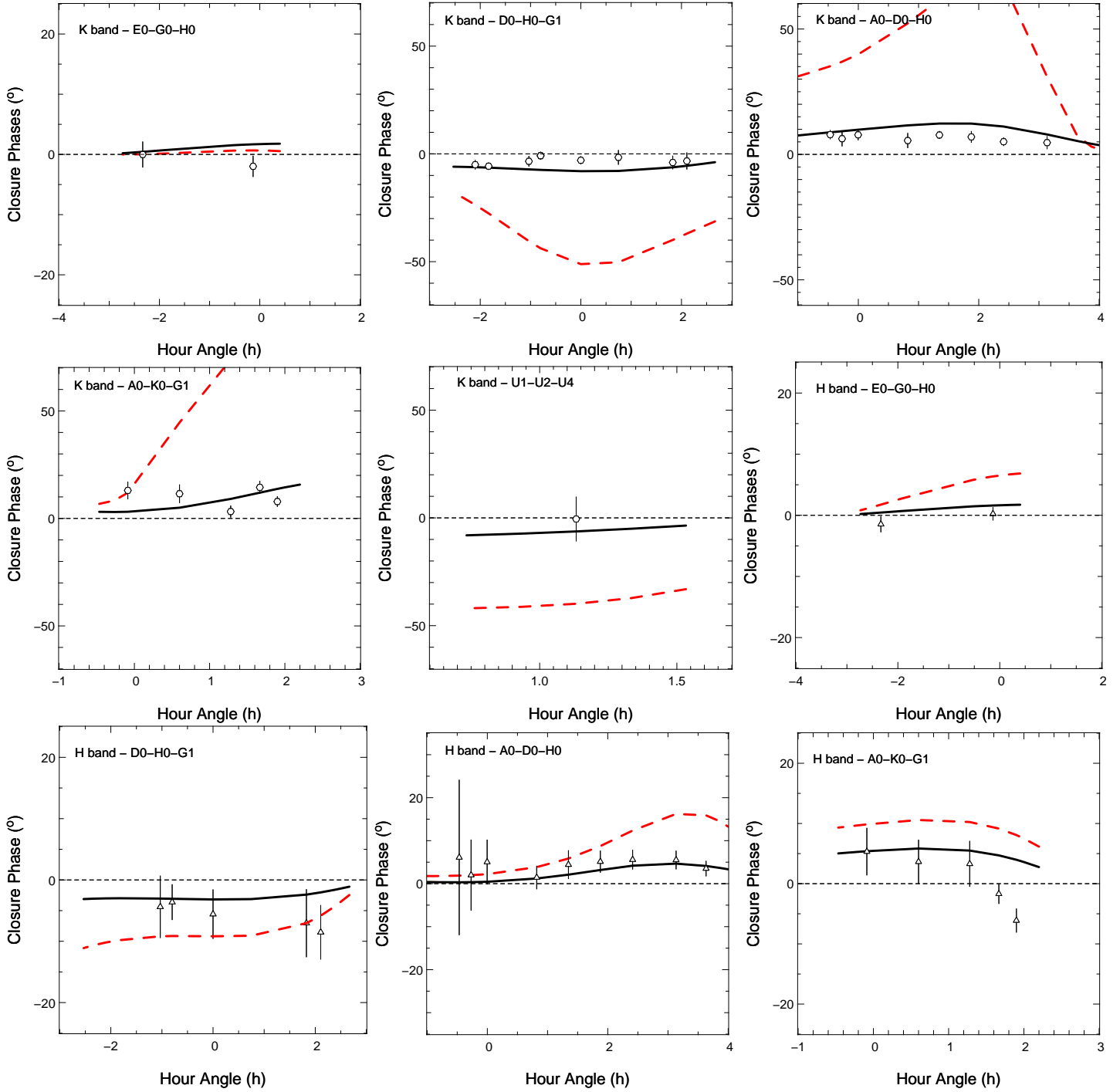


Fig. 12. Closure phases versus hour angle. In each panel, the predictions of the disk rim model (dashed red lines) and our model that includes iron grains (full black line) are overplotted. The corresponding telescope configuration and wavelength band are indicated in the upper left corners. The K band and H band measurements are plotted with circles and triangles, respectively.

We suggest instead that a small fraction of refractory grains survive very close to the star. We propose models for the optically thin emission of the innermost region, using various kinds of refractory grains, distributed from 0.10 AU to 0.45 AU. The dust surface density provides only a lower limit to the gas surface density, as we do not know the exact nature of the grains nor their abundance. However, we find that a low density region is consistent with the location and properties of the rim, as condensation of silicates will occur, and with the lack of molecular features in the spectrum of HD 163296. In fact, we expect

the gas in the inner disk to be mostly atomic, in non-LTE, and although its continuum emission will be small, hydrogen lines can be strong. The models used in Sect. 4.5.2 to argue for the presence of refractory grains, make a number of crude assumptions and improved models that self-consistently compute the grain temperature and emission in the thin disk as well as the properties of the rim are being developed. Our study indicates that the inner region of HD 163296 is quite empty, with a very low surface density that is incompatible with a dense accretion disk. For comparison, a surface density of 1 g/cm^2 at $\sim 0.10 \text{ AU}$

corresponds, in a standard accretion disk ($\alpha=0.01$), to an accretion rate of $\sim 10^{-11} M_{\odot}\text{yr}^{-1}$, much lower than typical values of Herbig Ae stars (Garcia Lopez et al. 2006). We do not constrain with our data the outer radius of this low density region, which can be larger than 0.5 AU. However, we know that at large radii the HD 163296 disk is massive and dense, as shown by the millimeter interferometric observations of Isella et al. (2007). It seems likely that HD 163296 has a dense disk with an inner cavity, and that we are observing it just before it reaches the transition disk phase, as suggested by Sitko et al. (2008).

It is fair to stress that we make no claim that our interpretation is unique. As stated at the beginning of Sect. 4, we assumed that the NIR emission of HD 163296, at spatial scales of less than 0.5 AU, is dominated by the emission of a circumstellar disk. Moreover, we interpreted the non-zero values of the CP as evidence of the asymmetric emission of a disk rim. While the properties that we derived for the smooth inner emission are probably robust, the presence of the rim is less so. In particular, the lack of visibility bounces at large baselines argues against the presence of a rim. In this case, the observed closure phases could possibly be explained by any asymmetric brightness distribution, such as a symmetric flared disk with a stellar contribution that is off-centered by few percent of the inner disk radius with respect to the disk (Malbet et al. 2001), by a hot spot on the disk, or by a density discontinuity. Only a larger (u, v) coverage, giving access to more details of the morphology could solve this ambiguity.

Our interpretation of the smooth, inner emission as coming from refractory grains requires their survival to very high temperatures (~ 2100 – 2300 K), much higher than expected even for the most refractory grains at the pressure of the low-density inner disk (Pollack et al. 1994; Kama et al. 2009). However, clearing of the innermost regions and optically thin emission from left-over refractory grains could be a common phenomenon in Herbig Ae stars. Their presence in the first few tenths of an AU could be a very seducing explanation to the observed depletions in refractory dust species – such as iron – in jets of young stars that are launched from this region (Nisini et al. 2005; Podio et al. 2006). Similar interferometric studies, with a large number of measurements in various wavelength bands simultaneously, should be done on a large sample of stars. A higher level of complexity in models is also needed to account for both the dust and the gas emission in a self-consistent way. Finally, the advent of the next-generation imaging instruments will hopefully bring unambiguous constraints on these complex environments.

Acknowledgements. We acknowledge fundings from CNRS and INAF (grant ASI-INAF I/016/07/0). This work was in part performed under contract with the Jet Propulsion Laboratory (JPL) funded by NASA through the Michelson Fellowship Program. JPL is managed for NASA by the California Institute of Technology. We thank A. Sargent and T. Ray for hosting part of this research, and the VLTI team at Paranal for the help in obtaining these data. We thank J.D. Monnier who provided with the IOTA data, and M. Sitko for discussions about the photometric measurements. We are grateful to A. Crida, M. Desort and S. Renard for fruitful discussions. We acknowledge the anonymous referee for his comments that improved the clarity of the paper.

References

Begemann, B., Dorschner, J., Henning, T., et al. 1997, *ApJ*, 476, 199
 D'Alessio, P., Calvet, N., & Hartmann, L. e. a. 1999, *ApJ*, 527, 893
 de Winter, D., van den Ancker, M. E., Maira, A., et al. 2001, *A&A*, 380, 609
 Deville, M., Bouret, J.-C., Catala, C., et al. 2005, *A&A*, 429, 247
 Devine, D., Grady, C. A., Kimble, R. A., et al. 2000, *ApJ*, 542, L115
 Doucet, C., Pantin, E., Lagage, P. O., & Dullemond, C. P. 2006, *A&A*, 460, 117
 Dullemond, C. P., Dominik, C., & Natta, A. 2001, *ApJ*, 560, 957
 Duschl, W. J., Gail, H.-P., Keller, C., & Tscharnutter, W. M. 1999, in *Astronomische Gesellschaft Meeting Abstracts*, Vol. 15, Astronomische Gesellschaft Meeting Abstracts, ed. R. E. Schielicke, 14–+
 Eisner, J. A. 2007, *Nature*, 447, 562
 Eisner, J. A., Chiang, E. I., Lane, B. F., & Akeson, R. L. 2007, *ApJ*, 657, 347
 Eisner, J. A., Graham, J. R., Akeson, R. L., & Najita, J. 2009, *ApJ*, 692, 309
 Eisner, J. A., Lane, B. F., & Hillenbrand, L. A. e. a. 2004, *ApJ*, 613, 1049
 Ferland, G. J., Korista, K. T., Verner, D. A., et al. 1998, *PASP*, 110, 761
 Garcia Lopez, R., Natta, A., Testi, L., & Habart, E. 2006, *A&A*, 459, 837
 Grady, C. A., Devine, D., Woodgate, B., et al. 2000, *ApJ*, 544, 895
 Günther, H. M. & Schmitt, J. H. M. 2009, *A&A*, 494, 1041
 Hillenbrand, L. A., Strom, S. E., Vrba, F. J., & Keene, J. 1992, *ApJ*, 397, 613
 Isella, A. & Natta, A. 2005, *A&A*, 438, 899
 Isella, A., Tatulli, E., Natta, A., & Testi, L. 2008, *A&A*, 483, L13
 Isella, A., Testi, L., & Natta, A. 2006, *A&A*, 451, 951
 Isella, A., Testi, L., Natta, A., et al. 2007, *A&A*, 469, 213
 Kama, M., Min, M., & Dominik, C. 2009, ArXiv e-prints
 Koike, C., Kaito, C., Yamamoto, T., et al. 1995, *Icarus*, 114, 203
 Kraus, S., Hofmann, K.-H., Benisty, M., et al. 2008a, *A&A*, 489, 1157
 Kraus, S., Preibisch, T., & Ohnaka, K. 2008b, *ApJ*, 676, 490
 Krugel, E. 2003, *Astronomy and Geophysics*, 44, 35
 Laor, A. & Draine, B. T. 1993, *ApJ*, 402, 441
 Le Bouquin, J.-B., Baudin, F., Hagenauer, P., et al. 2008, *A&A*, 481, 553
 Malbet, F., Lachaume, R., & Monin, J.-L. 2001, *A&A*, 379, 515
 Mannings, V. & Sargent, A. I. 1997, *ApJ*, 490, 792
 Meeus, G., Waters, L. B. F. M., Bouwman, J., et al. 2001, *A&A*, 365, 476
 Millan-Gabet, R., Malbet, F., Akeson, R., et al. 2007, in *Protostars and Planets V*, ed. B. Reipurth, D. Jewitt, & K. Keil, 539–554
 Millan-Gabet, R., Schloerb, F. P., & Traub, W. A. 2001, *ApJ*, 546, 358
 Miroshnichenko, A., Ivezić, Z., & Elitzur, M. 1997, *ApJ*, 475, L41+
 Monnier, J. D., Berger, J.-P., Millan-Gabet, R., et al. 2006, *ApJ*, 647, 444
 Monnier, J. D. & Millan-Gabet, R. 2002, *ApJ*, 579, 694
 Monnier, J. D., Millan-Gabet, R., Billmeier, R., et al. 2005, *ApJ*, 624, 832
 Montesinos, B., Eiroa, C., Mora, A., & Merín, B. 2009, *A&A*, 495, 901
 Muzerolle, J., D'Alessio, P., Calvet, N., & Hartmann, L. 2004, *ApJ*, 617, 406
 Najita, J. R., Carr, J. S., Glassgold, A. E., & Valenti, J. A. 2007, in *Protostars and Planets V*, ed. B. Reipurth, D. Jewitt, & K. Keil, 507–522
 Najita, J. R., Doppmann, G. W., & Carr, J. S. e. a. 2009, *ApJ*, 691, 738
 Najita, J. R., Edwards, S., Basri, G., & Carr, J. 2000, *Protostars and Planets IV*, 457
 Natta, A., Prusti, T., Neri, R., et al. 2001, *A&A*, 371, 186
 Natta, A., Testi, L., Neri, R., Shepherd, D., & Wilner, D. 2004, *A&A*, 416, 179
 Nisini, B., Bacciotti, F., Giannini, T., et al. 2005, *A&A*, 441, 159
 Pauls, T. A., Young, J. S., Cotton, W. D., & Monnier, J. D. 2005, *PASP*, 117, 1255
 Petrov, R. G., Malbet, F., Weigelt, G., et al. 2007, *A&A*, 464, 1
 Podio, L., Bacciotti, F., Nisini, B., et al. 2006, *A&A*, 456, 189
 Pollack, J. B., Hollenbach, D., Beckwith, S., et al. 1994, *ApJ*, 421, 615
 Posch, T., Kerschbaum, F., Fabian, D., et al. 2003, *ApJS*, 149, 437
 Schöller, M. 2007, *New Astronomy Review*, 51, 628
 Sitko, M. L., Carpenter, W. J., Kimes, R. L., et al. 2008, *ApJ*, 678, 1070
 Swartz, D. A., Drake, J. J., Elsner, R. F., et al. 2005, *ApJ*, 628, 811
 Tannirkulam, A., Harries, T. J., & Monnier, J. D. 2007, *ApJ*, 661, 374
 Tannirkulam, A., Monnier, J. D., Harries, T. J., et al. 2008, *ApJ*, 689, 513
 Tatulli, E., Millour, F., Chelli, A., et al. 2007, *A&A*, 464, 29
 van den Ancker, M., de Winter, D., & Tjin A Djie, H. 1998, *A&A*, 330, 145
 Vinković, D., Ivezić, Ž., Jurkić, T., & Elitzur, M. 2006, *ApJ*, 636, 348
 Wassell, E. J., Grady, C. A., & Woodgate, B. e. a. 2006, *ApJ*, 650, 985
 Weingartner, J. C. & Draine, B. T. 2001, *ApJ*, 563, 842